Real-Time Inference of Stochastic Damage in Composite Materials

E. E. Prudencio, P. T. Bauman, S. V. Williams,
D. Faghihi, K. Ravi-Chandar*, and J. T. Oden

Institute for Computational Engineering and Sciences (ICES)
The Department of Aerospace Engineering and Engineering Mechanics
The University of Texas at Austin
201 East 24th St, Stop C0200, Austin, Texas 78712-1229, USA

Abstract

This study describes a control system designed for real-time monitoring of damage in materials that employs methods and models that account for uncertainties in experimental data and parameters in continuum damage mechanics models. The methodology involves (1) developing an experimental set-up for direct and indirect measurements of damage in materials; (2) modeling damage mechanics based constitutive equations for continuum models; and (3) implementation of a Bayesian framework for statistical calibration of model with quantification of uncertainties. To provide information for real-time monitoring of damage, indirect measurement of damage is made feasible using an embedded carbon nanotube (CNT) network to perform as sensor for detecting the local damage. A software infrastructure is developed and implemented in order to integrate the various constituents, such as finite element approximation of the continuum damage models, generated experimental data, and Bayesian-based methods for model calibration and validation. The outcomes of the statistical calibration and dynamic validation of damage models are presented. The experimental program designed to provide observational data is discussed.
Keywords: *A. Nanotube; C. Damage mechanics; C. Finite element analysis (FEA); C: Bayesian analysis; D. Damage detection.*

1 Introduction

The use of computational models that interact dynamically with systems that deliver observational data, so as to predict the behavior of physical systems has been the central strategy of many technologies, ranging from weather and climate prediction to so-called smart materials. A higher-level version of such system executes controls that are designed to change the behavior of the system in near real time to react to changes in data. The success of such dynamic data-driven systems strongly depends upon the validation of the models, the

*Corresponding author, Center for Mechanics of Solids, Structures and Materials, The University of Texas at Austin, Austin, TX 78712-0235, USA.
E-mail address: kravi@mail.utexas.edu.

calibration, and how well uncertainties in data, model parameters, and quantities of interests (e.g. control variables) are quantified.

In the early days of damage monitoring, the focus was on nondestructive evaluation using inspection techniques such as visual observations (e.g. [21, 6]), ultrasonic waves or x-rays (e.g. [1]), infrared thermography (e.g. [26, 10, 20]), electrical resistance measurement (e.g. [40, 32]) and other methods to reveal the damage state. These techniques are used during periodic interruptions of service of the structure. Recent advances have altered this methodology to embed sensors or sensor arrays into the structure and perform continuous acquisition of data that are interpreted in terms of evolving damage. This is called structural health monitoring [23, 25].

In the present investigations, we describe a new system of this type, designed to monitor material damage as a prelude to structural failure which is embedded in emerging methodologies of model validations, Bayesian inferences, model selections, experimental mechanics, and computational mechanics. The system involves the identification of classes of parametric phenomenological models of material damage, dynamic (quasi-static) acquisition of data from a special methodology for detecting and monitoring damage, dynamic updating using a nonlinear version of Kalman filtering, all implemented in a Bayesian statistical framework. The ability to adopt the specific form of the damage model based on Bayesian model plausibilities is also included as part of the system; the general structures of the approach are laid out here. The details on computational algorithms are described in a companion paper [24].

Here, finite element models of material damage theories of the type used in contemporary fatigue analysis, fracture mechanics, and structural mechanics are employed. These typically involve material parameters that exhibit uncertainties and calculation of model plausibilities must enter as a key part of the prediction scheme. On the experimental side, an experimental program for monitoring damage is set up which itself can involve uncertainties due to the experimental issues. A network of Carbon Nano-Tubes (CNT) embedded in the matrix of the composite is used to detect damage. Local damage in the form of micro-cracks is signaled by local changes in the electric field and is manifested as a change in the effective resistivity of the material. Correlation of this change to damage is explored through direct measurements of the strain field as well as the resistivity. Thus, this system itself must also be calibrated and validated, and the inherent uncertainties in data must be factored into a statistical analysis for the validation of the full system.

In the present study, uniaxial tensile experiments are conducted on specimens of composite materials. The information for real-time monitoring of damage, is provided through indirect measurements of damage using the sensors enabled through embedded carbon nanotube CNT network detecting the local damage. However, the data corresponding to the continuum damage mechanics model parameters and to the experimental measurements are generally incomplete, unknown, and/or contains uncertainties. Such deficiencies are addressed through a predictive computational modeling framework. A statistical calibration is conducted in which probability densities of random model parameters and modeling errors in the theoretical structure are estimated using low-level measurement data. Particularly, Bayesian approaches, based on contemporary treatments of statistical inverse analysis [2, 3, 13, 29, 41] are employed. One advantage of such general approach is that it provides an all-inclusive framework for identifying the essential features of a predictive model as well as providing means to characterize uncertainty. The main feature is that the theoretical

model, model parameters, and experimental observations are not deterministic. Assigning random variables or processes characterized by probability density functions (PDF's) to the aforementioned variables, transforms the model into a stochastic problem. In addition, a software infrastructure is developed [24] and implemented in order to integrate experimental data with the finite element solution of the continuum damage mechanics model in order to calibrate the model based on the Bayesian statistical inverse methods.

2 Continuum Damage Mechanics

A material under loading is regarded as damaged relative to some initial state when it experiences a loss of stiffness due to the emergence of microscale defects (e.g. micro-cracks, micro-voids). Kachanov[12] has pioneered the concept of continuum damage mechanics, where he introduced a scalar measure characterizing the density of the micro-defects in the material. More general models of anisotropic damage were introduced by Chaboche[4, 5], Murakami and Ohno [22], and Krajcinovic and Foneska [16], in which the damage variable can be tensorial. The theory of continuum damage mechanics is extended later for ductile materials and composites, in which the damage variable (scalar or tensor) replicates the different types of degradation at the micro-scale level, such as nucleation and growth of voids, cracks, cavities, micro-cracks, and other microscopic defects [34, 7, 33, 17]. Moreover, the concept of fabric tensors introduced by Kanatani [14] to describe microstructural anisotropy, is applied to crack distribution and damage mechanics [19, 36]. This approach has been shown to be important in accounting for the qualitative and quantitative effects of defects on the stiffness of fiber-reinforced composite materials [36, 37, 39, 38, 35]. Here we restrict ourselves to isotropic damage, which consists of cracks and cavities with an orientation distributed uniformly in all directions. In this case, the damage variable does not depend on the orientation and the damaged state is completely characterized by the scalar D; in this case, where $D = 0$ characterizes the virgin (undamaged) state, while $D = 1$ characterizes the initiation of a macro-crack and complete rupture. In fact, fracture or complete rupture mostly occurs when $D = D_c \leqslant 1$, where D_c is the critical damage density, which is a material property. The parameter D_c is usually taken between 0.2 and 0.8 for engineering materials (see the references in Lemaître and Chaboche [18]).

Often, plastic deformation has a major influence on the damage evolution and conversely. The distinction between the two physical phenomena is well-known and is demonstrated in Figure 1, which shows the stress-strain responses of a bar of uniform cross section subjected to an uniaxial loading-unloading history. In this figure, E the initial elastic modulus is constant and $\bar{E}$ represents the effective elastic modulus that varies with the evolution of damage (i.e. $\bar{E} = E$ for no damage case). Although the damage process is a thermodynamically irreversible deformation, it is generally assumed that the deformation due to damage itself can be completely recovered upon unloading. Thus, the recoverable part of the strain, ϵ^e, is attributed to crack closure upon unloading and only causes degradation in the material stiffness, while the unrecoverable part, ϵ^p, is attributed to plasticity that causes permanent deformation. A general framework for modeling the coupled elasto-plastic and damage material behavior is outlined in this section.

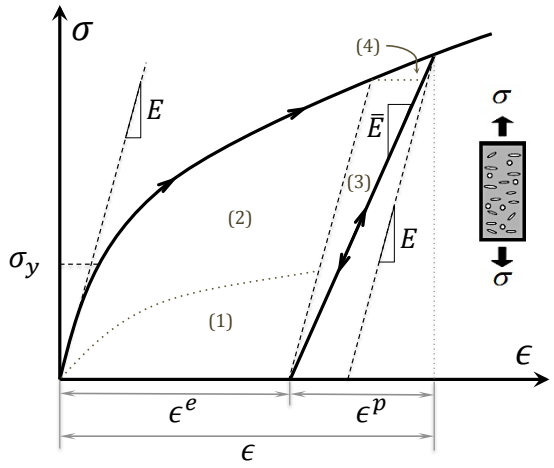

Figure 1: Idealized 1D stress–strain relation showing loss in stiffness due to material damage and permanent plastic strain after unloading. Different types of energy are recognized in this figure for the area under the stress - strain curve: (1) stored energy due to plastic hardening; (2) dissipated energy as heat by plastic work; (3) stored energy due to damage hardening; (4) dissipated energy as heat during the formation of the damage.

2.1 Basic Equations

We begin by selecting a class of parametric models of the quasi-static behavior of structural materials which embodies isotropic damage and strain-hardening plasticity emanating from a linearly-elastic isotropic material. The governing equations, which are assumed to be posed on a bounded domain $\Omega \subset \mathbb{R}^3$ with smooth boundary $\partial\Omega$ are

$$\boldsymbol{\nabla}.\boldsymbol{\sigma}(\mathbf{x},t) + \mathbf{f}(\mathbf{x}) = 0, \qquad \forall\ \mathbf{x} \in \Omega \quad \text{and} \quad t > 0, \tag{1}$$

and

$$\boldsymbol{\sigma}(\mathbf{x},t) = \boldsymbol{\sigma}(\mathbf{x},t)^T, \qquad \forall\ \mathbf{x} \in \Omega \quad \text{and} \quad t > 0, \tag{2}$$

along with the traction condition,

$$\mathbf{g}(\mathbf{x},t) = \boldsymbol{\sigma}(\mathbf{x},t)\mathbf{n}, \qquad \forall\ \mathbf{x} \in \Gamma_\sigma, \tag{3}$$

where $\boldsymbol{\sigma}(\mathbf{x},t)$ is the Cauchy stress at point $\mathbf{x}$ on Ω at time t, $\mathbf{f}(\mathbf{x})$ is body force acting within Ω, $\mathbf{g}(\mathbf{x},t)$ are prescribed tractions on surface $\Gamma_\sigma \subset \partial\Omega$, and $\mathbf{n}$ denotes the outward unit normal to $\partial\Omega$.

Considering the additive decomposition of strain tensor[1],

$$\boldsymbol{\epsilon} = \frac{1}{2}\left(\boldsymbol{\nabla}\mathbf{u} + (\boldsymbol{\nabla}\mathbf{u})^T\right), \tag{4}$$

into elastic, $\boldsymbol{\epsilon}^e$, and plastic, $\boldsymbol{\epsilon}^p$, along with the loss of elastic stiffness due to material damage, the *reduced stress tensor* and the *effective elastic energy density* can be expressed respectively as,

[1] where $\boldsymbol{\nabla}\mathbf{u}$ is the displacement gradient

$$\boldsymbol{\sigma} = (1 - D)\, \mathbb{C}\, (\boldsymbol{\epsilon} - \boldsymbol{\epsilon}^p), \tag{5}$$

and

$$Y = (\boldsymbol{\epsilon} - \boldsymbol{\epsilon}^p) : \mathbb{C}(\boldsymbol{\epsilon} - \boldsymbol{\epsilon}^p), \tag{6}$$

where $\mathbb{C}$ is the fourth-order elasticity tensor, $\boldsymbol{\epsilon}$ is the strain tensor, and $\boldsymbol{\epsilon}^p$ is the plastic strain tensor.

Following standard arguments, a weak or variational form of the elasto-plasto-damage model can then be constructed as follow:
Find $\mathbf{u}(t) \in \mathcal{V}, t \in [0, T)$ such that

$$\int_\Omega (1 - D)\, \mathbb{C}\, (\boldsymbol{\epsilon} - \boldsymbol{\epsilon}^p)\ :\ \nabla \boldsymbol{v}\, \mathrm{d}x = \int_\Omega \mathbf{f}\ .\ \boldsymbol{v}\, \mathrm{d}x\ +\ \int_{\Gamma_\sigma} \mathbf{g}\ .\ \boldsymbol{v}\, \mathrm{d}s, \qquad \forall\ \boldsymbol{v} \in \mathcal{V} \tag{7}$$

for an appropriate space of test functions, $\boldsymbol{v}$,

$$\mathcal{V} = \{\boldsymbol{v}(\mathbf{x}) \mid \boldsymbol{v}(\mathbf{x}) \in H^1(\Omega)\ ;\ \boldsymbol{v}(\mathbf{x}) = 0,\ \forall\ \mathbf{x} \in \Gamma_u\}, \tag{8}$$

where H^1 is the Sobolev space of functions with first-order generalized derivatives in $L^2(\Omega)$.

2.2 Constitutive Relations

Here the Mises-Hill flow rule is taken into account for the constitutive description of plastic flow. Therefore the form for the non-negative and convex rate of dissipation is postulated as,

$$\mathscr{D} = \mathcal{Y}(p)\, |\dot{\boldsymbol{\epsilon}}^p| + \omega(D)\, \dot{D}, \tag{9}$$

where $\mathcal{Y}$ is flow resistance which is a function of the accumulated plastic strain ($p = |\boldsymbol{\epsilon}^p|$) and ω represents the threshold of damage which is a function of the damage variable D.

Making use of co-directionality hypothesis,

$$\mathbf{N}^p = \frac{\boldsymbol{\tau}}{|\boldsymbol{\tau}|} = \frac{\dot{\boldsymbol{\epsilon}}^p}{|\dot{\boldsymbol{\epsilon}}^p|}, \tag{10}$$

where the flow direction is denoted by $\mathbf{N}^p$ and deviatoric part of stress is denoted by $\boldsymbol{\tau} = (\boldsymbol{\sigma} - \frac{1}{3}(\mathrm{tr}\boldsymbol{\sigma})\mathbf{I})$, the boundedness inequalities for plasticity and damage can be written as,

$$|\boldsymbol{\tau}| \leq \mathcal{Y}(p), \tag{11}$$

$$Y \leq \omega(D). \tag{12}$$

The functional form of the flow resistance is given by summation of a constant and strictly positive yield stress, σ_Y, and isotropic hardening, R, which is a function of accumulated plastic strain:

$$\mathcal{Y}(p) = \sigma_Y + \mathcal{R}(p). \tag{13}$$

For isotropic hardening a simple power law including two material parameters, B and m, is considered here ,

$$\mathcal{R}(p) = Bp^m. \tag{14}$$

Several evolution equations exist in the literature for damage that provide different functions ω for predicting the material failure. Krajcinovic and Foneska [16] postulated the following power law for the damage evolution in brittle materials,

$$\dot{D} = (s+1)\frac{\epsilon^s}{\epsilon_{\mathrm{R}}^{(s+1)}}\dot{\epsilon}, \tag{15}$$

where s is a material constant and ϵ_{R} can be interpreted as the final strain at rupture. Such evolution equation results in the following damage threshold, which is referred to as the Krajcinovic Damage Model throughout this paper:

$$\omega(D) = \frac{1}{2}E\epsilon_{\mathrm{R}}^2 D^{\left(\frac{2}{s+1}\right)}. \tag{16}$$

2.3 Finite Element Approximation

Introducing the constitutive relationships into the momentum equation (1), over the time interval $0 = t_0 < t_1 < \cdots < t^{(k)} < t^{(k+1)} < \ldots$, leads to the following governing equations (in the absence of body forces),

$$\left.\begin{array}{rcll} \boldsymbol{\nabla}.\boldsymbol{\sigma}^{(k+1)} & = & 0 & \forall\ \mathbf{x} \in \Omega, \\ \mathbf{u}^{(k+1)} & = & \mathbf{u}_0(\mathbf{x}, t^{(k+1)}) & \forall\ \mathbf{x} \in \Gamma_u, \\ \boldsymbol{\sigma}^{(k+1)}\mathbf{n} & = & \mathbf{g}_0(\mathbf{x}, t^{(k+1)}) & \forall\ \mathbf{x} \in \Gamma_\sigma, \end{array}\right\}, \tag{17}$$

where stress and displacement at point $\mathbf{x} \in \Omega$ and at time $t^{(k+1)}$ are denoted by $\boldsymbol{\sigma}^{(k+1)}(= \boldsymbol{\sigma}(\mathbf{x}, t^{(k+1)}))$ and $\mathbf{u}^{(k+1)}(= \mathbf{u}(\mathbf{x}, t^{(k+1)}))$. Therefore from (7), one can arrive at the incremental equation

$$\int_\Omega (1 - D^{(k+1)})\, \mathbb{C}\, (\boldsymbol{\epsilon}^{(k+1)} - \boldsymbol{\epsilon}^{p\,(k+1)})\ :\ \nabla \boldsymbol{v}\ \mathrm{d}x = \int_{\Gamma_\sigma} \mathbf{g}_0(\mathbf{x}, t^{(k+1)})\ .\ \boldsymbol{v}\ \mathrm{d}s, \qquad \forall\ \boldsymbol{v} \in \mathcal{V}. \tag{18}$$

Finite element approximation of (18) is constructed following standard procedure. In the above relations, the unknowns are the displacement $\mathbf{u}$, the plastic strain $\boldsymbol{\epsilon}^p$, and the damage variable D.

The stress state evaluation is achieved by discretizing the evolution equations of the stress and damage. Under quasi-static loading, one will work with increments, e.g. $\Delta\boldsymbol{\epsilon}$, as opposed to an unsteady discretization in time. Thus, given a displacement increment $\dot{\mathbf{u}} \approx \Delta\mathbf{u} = \mathbf{u}^{(k+1)} - \mathbf{u}^{(k)}$, one can compute the corresponding strain increment $\dot{\boldsymbol{\epsilon}} \approx \Delta\boldsymbol{\epsilon} = \boldsymbol{\epsilon}^{(k+1)} - \boldsymbol{\epsilon}^{(k)}$.

Therefore, the integration scheme can be written as follows,

$$\begin{aligned}
&\boldsymbol{\epsilon}^{(k+1)} = \boldsymbol{\epsilon}^{(k)} + \Delta\boldsymbol{\epsilon}^{(k+1)},\\
&\boldsymbol{\sigma}^{(k+1)} = (1 - D^{(k+1)})\, \mathbb{C}\, (\boldsymbol{\epsilon}^{(k+1)} - \boldsymbol{\epsilon}^{p\,(k+1)}),\\
&Y^{(k+1)} = \tfrac{1}{2}(\boldsymbol{\epsilon}^{(k+1)} - \boldsymbol{\epsilon}^{p\,(k+1)}) : \mathbb{C}\, (\boldsymbol{\epsilon}^{(k+1)} - \boldsymbol{\epsilon}^{p\,(k+1)}),\\
&\boldsymbol{\epsilon}^{p\,(k+1)} = \boldsymbol{\epsilon}^{p\,(k+1)} + \Delta\boldsymbol{\epsilon}^{p\,(k+1)},\\
&p^{(k+1)} = p^{(k)} + \Delta p^{(k+1)},\\
&D^{(k+1)} = D^{(k)} + \Delta D^{(k+1)},
\end{aligned} \tag{19}$$

together with the consistency conditions

$$\begin{aligned}
&|\boldsymbol{\tau}^{(k+1)}| - \sigma_Y - \mathcal{R}(p^{(k+1)}) \leq 0,\\
&Y^{(k+1)} - \omega(D^{(k+1)}) \leq 0.
\end{aligned} \tag{20}$$

To insure the aforementioned consistency conditions, an implicit Backward Euler method is utilized for both plasticity and damage. The increment in accumulated plastic strain and the value of the damage variable in the Newton iterative procedure is obtained by solving the following algebraic system of equations:

$$\begin{bmatrix} \delta p^{(k+1)} \\ \Delta D^{(k+1)} \end{bmatrix} = -[K^{(k+1)}]^{-1} \begin{bmatrix} r_P^{(k+1)} \\ r_D^{(k+1)} \end{bmatrix}, \tag{21}$$

where δp is the increment on accumulated plastic strain. The residual setting using the consistency conditions can be obtained as follows,

$$r_P^{(k+1)} = |\boldsymbol{\tau}^{(k+1)}| - \sigma_Y - \mathcal{R}(p^{(k+1)}), \tag{22}$$

$$r_D^{(k+1)} = -D^{(k+1)} + D^{(k)} + \frac{\Delta Y^{dis(k+1)}}{\omega'\,(D^{(k+1)})}, \tag{23}$$

where $\omega' = \frac{\partial \omega}{\partial D}$ and the Jacobian matrix can be defined such as:

$$[K^{(k+1)}] = \begin{bmatrix} \partial r_P^{(k+1)}/\partial \Delta p^{(k+1)} & \partial r_P^{(k+1)}/\partial D^{(k+1)} \\ \\ \partial r_D^{(k+1)}/\partial \Delta p^{(k+1)} & \partial r_D^{(k+1)}/\partial D^{(k+1)} \end{bmatrix}. \tag{24}$$

3 Experiments

Our experimental program has two basic components. The first involves uniaxial tensile experiments with different load levels for measuring strain variation over the length of the

specimens. This is used to generate distributed damage in different parts of the specimen. These experiments are used for calibrating the continuum damage models. A second group of experiments are also performed with quasi-static loads for measuring electric potential variation along the length of the specimen, and for dynamically measuring damage in real-time using changes in electrical conductivity. The latter step requires relating changes in electrical conductivity to damage through a set of calibration experiments.

The process of formulating a conducting epoxy is quite complex. For this study, a commercially available solution was pursued. First, a bisphenol-A mixed with 2% by weight of CNT that was dispersed uniformly within the resin was obtained from Molecular Rebar of Austin, TX; this material had a well dispersed structure resulting in a rather high resistivity and could not be used to determine variations in resistivity with strain or damage. Then a second option was considered: Nanocyl S.A., produces a carbon nanotube enriched epoxy called Epocyl. The formulation used in this study is designated as Epocyl NC E128-02 and is composed of 80 wt% Epoxy resin (Bisphenol-A-epichlorhydrin) and 20 wt% Carbon nanotubes. The raw product has the texture of a paste due to the high concentration of carbon nanotubes, unlike a commercial resin.

The mixing process begins by selecting the ratio of Epocyl to Bisphenol-A for the desired conductivity and calculating the amount of epoxy mixture needed to fill the mold. Once these values are obtained, the required amount of Epocyl is taken and heated to soften the material so it can be mixed easily. The appropriate amount of Bisphenol-A is added and the mixture is repeatedly stirred and heated to obtain an evenly distributed product. Once well mixed, the product is placed under vacuum to evacuate the air bubbles introduced during stirring. The hardener is then added in a 1:5 ratio with the bulk Epocyl/Bisphenol-A mixture and stirred slowly to avoid additional air bubbles. The working time of the mixture once the hardener has been introduced is quite short, about 5 minutes, before the mixture becomes very viscous and can no longer be poured. The final mixture (carbon nanotube epoxy resin) is then slowly poured into the mold and left to cure for about 8 hours.

The plate is then cut into 0.6 inch strips; the rough edges of the strips are machined away using an endmill (3/8 inch) that brings the width of each strip down to 0.5 inch. Subsurface defects such as interior cracks, air bubbles, and unmixed epoxy regions are avoided during the machining process. To electrically insulate the sample from the metallic grips of the Instron testing machine, nonconductive plastic end tabs are attached to both ends of the specimen.

Uniaxial tensile loading experiments, interspersed with loading-unloading cycles, are performed on rectangular strip specimens. The global response of the specimen is characterized easily by measuring the force and extension. The spatial variation in the strain field (resulting from local perturbations in material state and properties) is measured at each load increment using digital image correlation [27]. In this method of strain measurement, the specimen is decorated by spray-painting a fine speckle pattern; this speckle pattern is imaged at high spatial resolution at each load increment. By comparing the speckle pattern in the initial and deformed specimen through a cross-correlation procedure, the displacement of each point within the specimen is identified, and the strain is then calculated. This method is very powerful and is used to determine strains over the entire surface of the specimen[2].

[2]The ARAMIS digital image correlation system supplied by Gom, Germany is used to perform these

In parallel with this experiment, the change in resistivity along the specimen length is monitored using a Keithly Model 6517 Electrometer. Such variations in resistivity are postulated to be the result of the changes in the microstructure due to breaking of the CNTs embedded inside the polymer matrix by the formation of matrix cracks. These resistivity measurements can be performed at a local level. The strategy is to consider the specimen as a resistor network, with varying resistances along the length; as the material damages, the resistivity is expected to increase, although there are contradictory reports in the literature [30, 31, 11]. Figure 2 shows the electrical measurement set up. As in the mechanical part, the specimen is considered to have inhomogeneities and therefore fluctuations in the resistance. The specimen is taken to be made of the same N segments of equal length $l_i = L/N,\ i = 1, 2, \ldots, N$[3]. Each segment may have different initial concentrations and distributions of CNTs and therefore the initial resistance can be written as:

$$R = (R_1, R_2, \ldots, R_N). \tag{25}$$

As illustrated in Figure 2(b) , the specimen can be viewed as a series-resistor network, through which the same current flows from a constant current source (with a voltage in the range 0-40 V). Therefore, by measuring the voltage drop over each region as well as the known current, one is able to calculate the resistivity changes in each segment.

The relationship between the changes in the resistances R and the damage, D can be obtained either through a calibration experiment or through a model of the CNT network. It is expeditious to begin with an experimental calibration and develop the model after identifying the underlying relationships more completely. As will be discussed in Section 5, although the fluctuations in the electrical resistivity are observed in course of uniaxial testing, two problems arise: first, the manufactured specimens do not show progressive damage, but more importantly, the resistivity changes are not well-correlated to the strain or damage field.

4 Model Calibration Under Uncertainties

A combination of the the continuum damage mechanics model (i.e. mathematical model) and its finite element discretization of Section 2 that provides the approximate solution of the damage model, results in a parametric class of *computational models* indexed by parameters vector $\boldsymbol{\theta} \in \mathbb{R}^{n_\theta}$, for some fixed positive integer $n_\theta > 0$, for each model in a set of models at our disposal (For the special case of using Krajcinovic Damage Model $n_\theta = 3$ and $\boldsymbol{\theta} = (E, s, \epsilon_{\mathrm{R}})$). This model is used in both forward and inverse problems.

In the case of an inverse problem, one needs to estimate the values of the model parameters $\boldsymbol{\theta}$ that cause computational model to best fit the given experimental data $\mathbf{d}$. In the case of a forward problem, the parameters $\boldsymbol{\theta}$ are given and one then needs to compute (i.e. predict) the quantity of interest.

However, many uncertainties are involved in the process of assessing the predictability of mathematical and computational models of the physical event:

measurements.

[3]In this experiment $N = 5$ is considered, which results in l_i of around 25 mm.

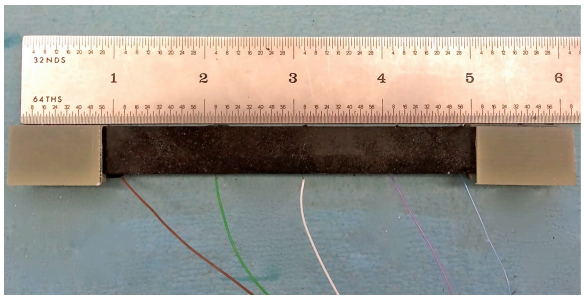

(a)

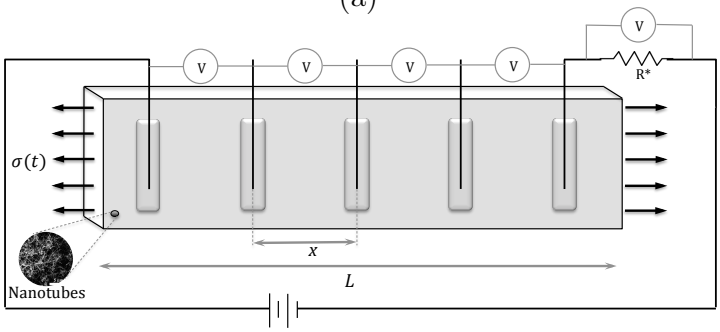

(b)

Figure 2: Typical electrical measurement set ups: (a) specimen with connected wires; (b) Schematic representation of showing the discretization of the specimen geometry,in order to determine conductivity/resistivity profile.

- the data is measured only at a small number of sample points of the system,
- the measured data has noise,
- the continuum damage mechanic models only approximates physical reality, and
- the computational model that maps the spatial distribution of resistivity to the spatial distribution of damage is also an imperfect characterization of reality.

The ingredients of the statistical calibrations problem are the data $\mathbf{d}(t)$ supplied by the experimental program at time t, the model parameters $\boldsymbol{\theta}$ for each choice of a model, the map of model parameters into observations, $\mathbf{y}(\boldsymbol{\theta}(t)) = \mathbf{d}(t) + \boldsymbol{\nu}(t)$, with $\boldsymbol{\nu}(t)$ being the experimental noise (assumed here to be normal distribution of zero mean and Σ^2 variance, $\mathcal{N}(0, \Sigma^2\mathbf{I})$), and prior information on parameters embedded in a probability density $\pi_{\text{prior}}(\boldsymbol{\theta}(t))$. The Bayesian update at time t_k is

$$\pi_{\text{post}}(\boldsymbol{\theta}(t_k)|\mathbf{d}(t_k)) = \frac{\pi_{\text{like}}(\mathbf{d}(t_k)|\boldsymbol{\theta}(t_k)) \cdot \pi_{\text{prior}}(\boldsymbol{\theta}(t_k))}{\pi_{\text{data}}(\mathbf{d}(t_k))}, \tag{26}$$

where $\pi_{\text{like}}(\mathbf{d}|\boldsymbol{\theta})$ is the likelihood probability density and $\pi_{\text{data}}(\mathbf{d})$ is the marginal density

$$\pi_{\text{data}}(\mathbf{d}) = \int \pi_{\text{like}}(\mathbf{d}|\boldsymbol{\theta}) \cdot \pi_{\text{prior}}(\boldsymbol{\theta}) \, \mathrm{d}\boldsymbol{\theta}. \tag{27}$$

The step-by-step implementation of (26) over set of time interval $[t_{k-1}, t_k]$, with the nonlinear likelihood calculated through a Newton algorithm, constitutes an extended Kalman filter, described in [24], and manages the entire statistical calibration of the system and real-time monitoring of damage using evolving data on damage.

5 Experimental Observations

The results of the experimental observations are reported in the following two sections. First, an evaluation of the variation of the resistivity with strain is explored. This is followed by experimental measurements of the distribution of strains in the specimen subjected to monotonic and cyclic loading.

5.1 Characterization of the Variation of Electrical Resistivity with Strain in CNT-Epoxy Specimens

The Epocyl composites with carbon nanotubes were evaluated for their resistivity properties using the experimental arrangement suggested in Section 3. As indicated earlier, there are conflicting reports on the effect of strain on resistivity and therefore, this work embarked on an experimental characterization of the response through uniaxial tests under creep, relaxation and cyclic loading conditions. The figures below show the corresponding results. In the relaxation experiment, the specimen is subjected to a nominal strain of 0.4%, and held fixed; the time variation of the load and the resistivity over the entire length of the specimen are monitored. As shown in Figure 3, the nominal stress (the load normalized by the cross-sectional area) decays from a little over 6 MPa to a little over 5 MPa in about 10,000 s. Corresponding to this, the resistivity – at constant strain – decays from about 4.45×10^6 Ω to about 4.35×10^6 Ω. The low frequency oscillations are the result of small fluctuations in the room temperature.

In the creep experiment, the load on the specimen is maintained at 200 N, and the extension of the specimen as well as the resistivity variation are monitored; as shown in Figure 4, the extension of the specimen increases from about 0.5 mm to 0.55 mm over about 10,000 s. Corresponding to this, the specimen resistivity decreases from about 4.7×10^6 Ω to about 4.5×10^6 Ω. These two sets of experiments suggest that the resistance always decreases, independently of whether the strain or stress is maintained constant. It is verified that there was no such relaxation of the resistance in the absence of the applied stress or strain, clearly indicating that the variation was driven by the imposed mechanical state. It should be noted that the drop in resistance during a stress relaxation test was about half of that observed during a creep test.

The response of the resistivity during ramp loading-unloading is shown in Figure 5. The resistance measuring scheme was first energized for about 10 minutes in order to reach a steady state, and then a ramp loading-unloading protocol was applied on the specimen, with continuous resistance monitoring. The loading rate was maintained at 1N.s^{-1}. As can be seen from Figure 5, at this very slow loading rate, the resistance increases monotonically and almost proportionally with the applied strain; however, upon strain reversal during unloading, a significantly hysteretic response is observed.

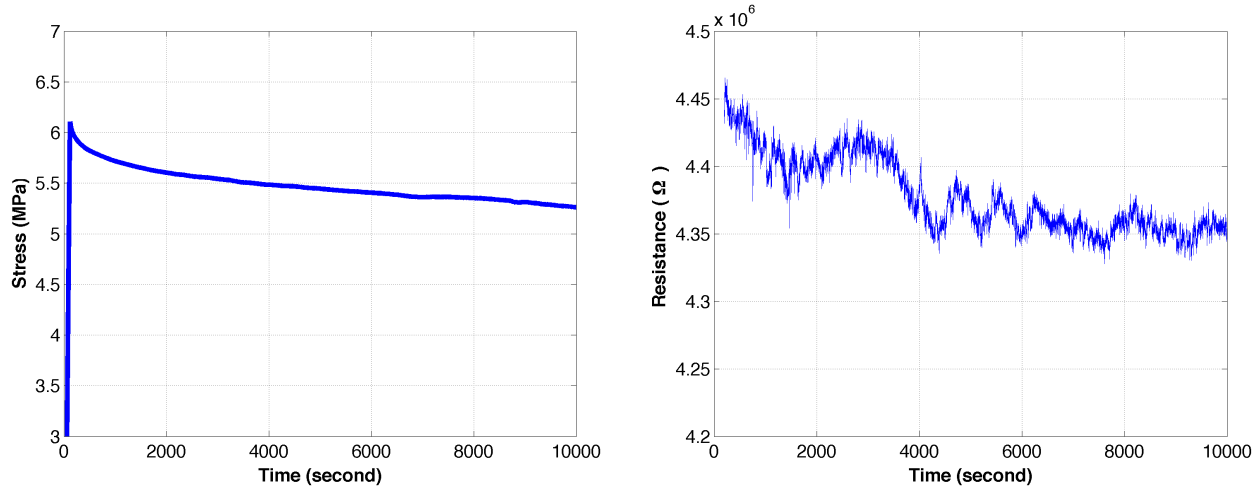

(a) (b)

Figure 3: Experimental characterization of the electrical in uniaxial tests under relaxation: (a) variation of stress with time; (b) variation of electrical resistance with time.

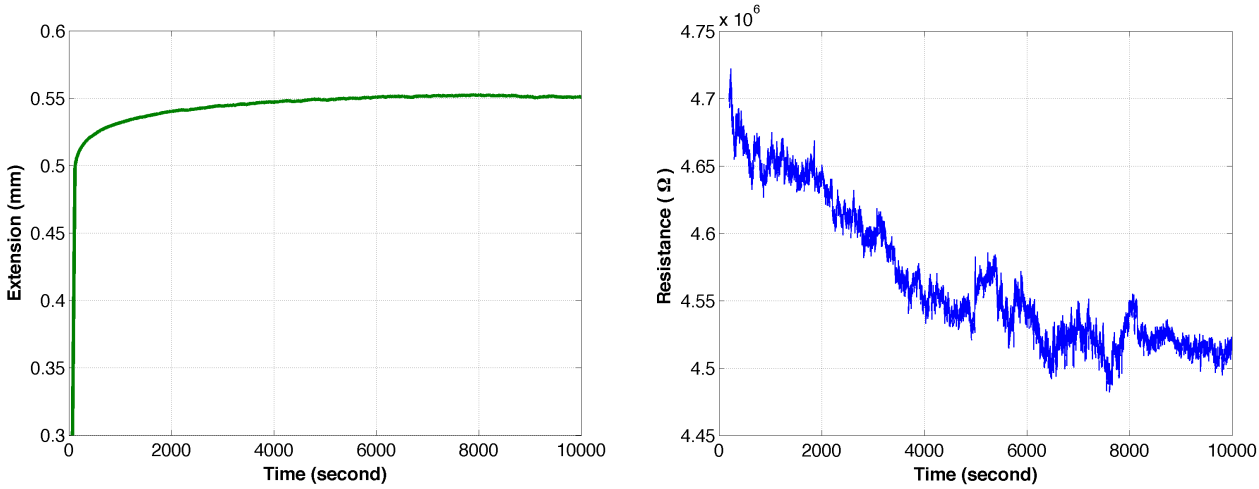

(a) (b)

Figure 4: Experimental characterization of the electrical in uniaxial tests under creep: (a) variation of extension with time; (b) variation of electrical resistance with time.

One final set of measurements was performed by following the wiring diagram shown in Figure 2. The resistance change in three different segments was measured as a function of the applied strain. It was found that the initial resistance in the different regions of the specimen was different due to fluctuation in the concentration of the CNT in the specimen; additionally, the change in resistance with strain also varied with location.

Collectively, these observations suggest that the underlying mechanisms that dictate the changes in resistance with position, strain and stress, as well as time-dependence are quite complex and require a much more in-depth examination before the CNT infiltrated epoxies can be used as diagnostic sensors. Perhaps this could be attempted in a future study.

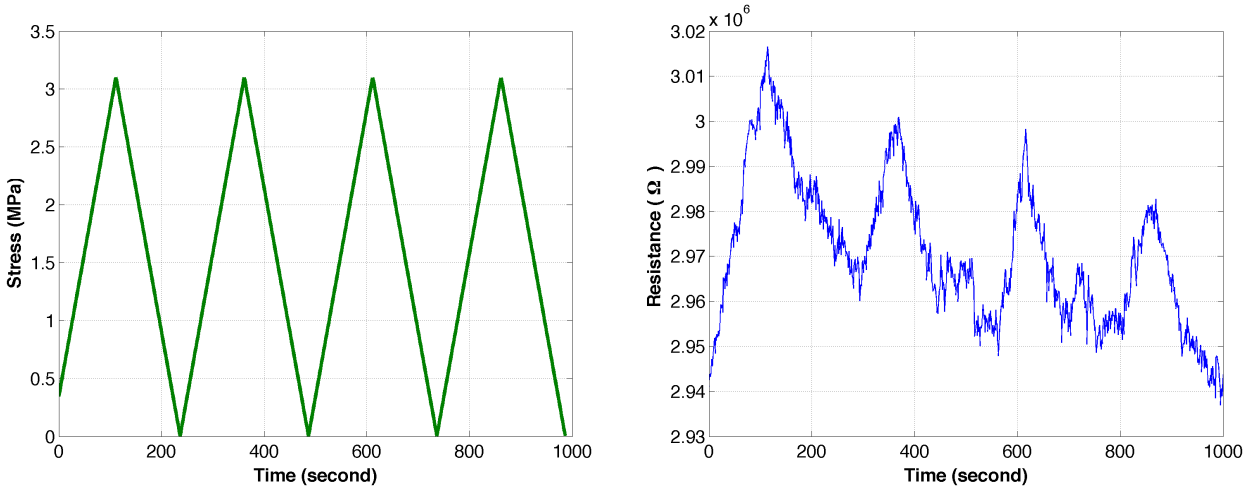

(a) (b)

Figure 5: Experimental characterization of the electrical in uniaxial tests under cyclic loading: (a) variation of stress with time; (b) variation of electrical resistance with time.

5.2 Characterization of the Variation of Strain with Cyclic and Monotonic Loading

A typical result from an experiment on CNT-Epoxy Specimens intended to calibrate the damage model is shown in Figures 6–9. Figures 6(a) shows the overall elongation $\Delta^k = \left|u(t^{(k)}, x_N) - u(t^{(k)}, x_0)\right|$ between the ends of the specimen; as indicated in the figure seven loading-unloading cycles were applied, with progressively greater displacement in each cycle. The specimen fractured (i.e. failed) in the last cycle. Figures 6(b) shows the corresponding overall load on the specimen as measured by the load cell; this corresponds to the data $f_{\text{exp}}(t^{(k)})$. The progression of damage in the specimen can be inferred by considering the variation of the overall specimen displacement Δ^k and load $f_{\text{exp}}(t^{(k)})$ as indicated in Figure 7; the nonlinearity experienced at strain levels greater than about 0.5% is an indication of inelastic response of the material that can be correlated to plasticity and/or damage.

Figure 8(a) shows a photograph of the specimen with an overlay of a contour plot corresponding to the local strain, ϵ at a particular step in the loading process when the average strain in the specimen was about 1.4%. Figure 8(b) shows the variation along x, the horizontal direction, of the strain at different times after beginning of the test (particularly at oneset of each unloading). These data correspond to $u(t^{(k)}, \mathbf{x})$, the measured displacement variation along x at time (i.e. load increment) k. There are two key features that are evident; first, while the average strain is about 1.4% in Figure 8(b), there is a background fluctuation over the entire length that arises from the noise in the process of digital image correlation used to evaluate the strains. Second, there are some hot-spots evident in Figure 8(b) where the strains are quite a bit higher than the average strain; these fluctuations are well above the noise in the measurements and correspond to points in the specimen where local defects trigger damage accumulation. Eventually, one of these hot-spots triggers failure of the specimen. This development of strain (or damage) accumulation is illustrated in Figure 9 where the spatial variation of strain in the specimen at $t = 493$ s is shown in Figure 9(a) and

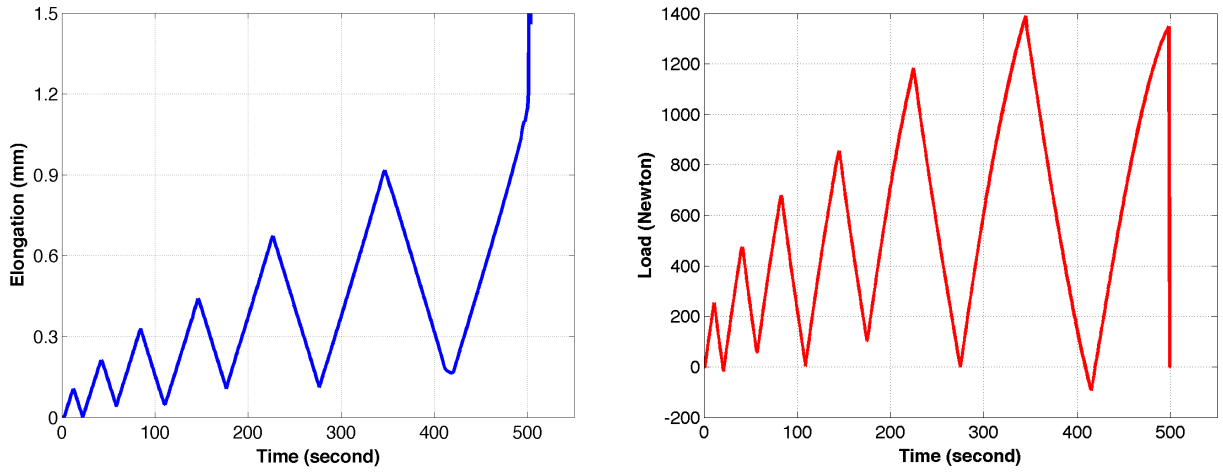

(a) (b)

Figure 6: Experimental results of the CNT-Epoxy specimen (applied displacement rate = 0.025mm.s^{-1}): (a) displacement variation with time measured by DIC; (b) load variation with time measured by the load cell.

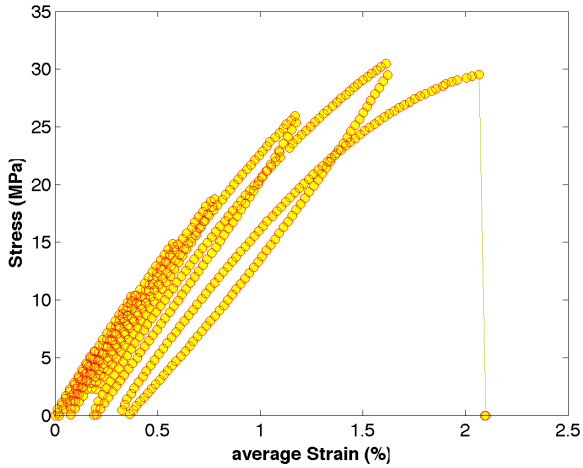

Figure 7: Nominal stress-strain response of the CNT-Epoxy specimen.

the comparison between the time variation of the strain in the uniform segment is shown in comparison to the strain in the hot-spot in Figure 9(b).

The measured displacement data $u(t^{(k)}, \mathbf{x})$, and the corresponding measured force $f_{\text{exp}}(t^{(k)})$ for all time steps, constitutes the experimental data set $\mathbf{d}(t^{(k)}, \mathbf{x}) = \left\{u(t^{(k)}, \mathbf{x}), f_{\text{exp}}(t^{(k)})\right\}$ to be used in calibration of the damage model. Based on the DIC resolution, the displacement data is measured in a grid that consists of 91 evenly-spaced points along x (i.e. $0 \leq i \leq 90$) and 17 points along y. Moreover, the DIC system is set to image the specimen with the rate of 1 image/second. Considering the total time of 500 s for conducting the test, the displacement and force are capture at 500 time steps (i.e. $0 \leq k \leq 500$).

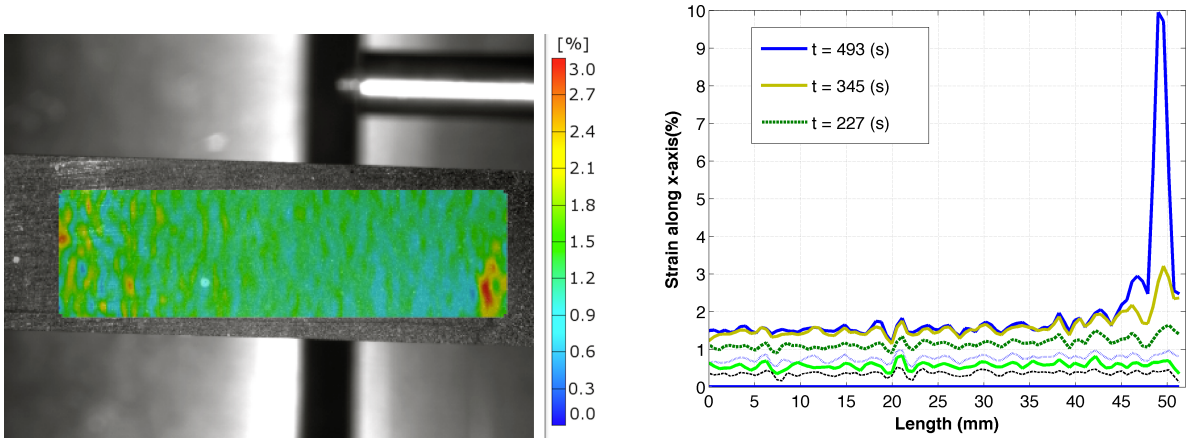

(a) (b)

Figure 8: Experimental results of the CNT-Epoxy specimen: (a) spatial variation of major strain in the specimen at $t = 493$ s; (b) the strain variation along x at different times (one set of unloading).

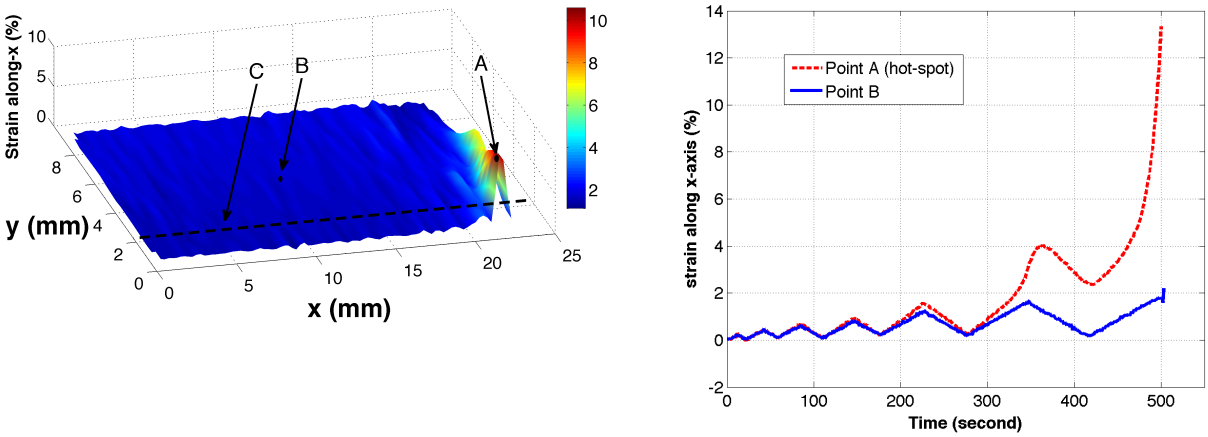

(a) (b)

Figure 9: Experimental results of the CNT-Epoxy specimen: (a) Spatial variation of strain at $t = 493$ s after beginning the test; (b) evolution of strain through time in the hot-spot and in the uniform segment (points A and B as shown (a) respectively)

6 Statistical Model Calibration and Real-Time Monitoring of Damage

6.1 General consideration

In order to calibrate the model parameters statistically against the experimental data, the finite element implementation of the Krajcinovic damage model (Section 2), the Bayesian

framework for statistical inverse problems (Section 4), and the generated experimental data on the nano-composite specimen (Section 5) are integrated into a software infrastructure. The libMesh library [15] is used for a parallel, C++ finite element implementation of the damage model. A one-dimentional finite element mesh is employed in the simulation of the center line of the high spatial resolution images of Figure 8 with averaging the strain measurements through the width of the specimen.

Here the initial knowledge regarding the Krajcinovic damage model parameters, $\boldsymbol{\theta} = (E, s, \epsilon_{\mathrm{R}})$, is assumed to reflect the proper range of each parameter defined as a uniform prior PDF. Therefore,

$$\pi_{\mathrm{prior}}(E) \sim \mathcal{U}\left(0.5e9, 0.5e10\right), \pi_{\mathrm{prior}}(s) \sim \mathcal{U}\left(-1, 10\right), \pi_{\mathrm{prior}}(\epsilon_{\mathrm{R}}) \sim \mathcal{U}\left(0.001, 1\right), \tag{28}$$

where $\mathcal{U}(B)$ is uniform distribution over a given set B.

The construction of the likelihood begins from the assumption that, if $\boldsymbol{\theta}$ are prescribed, the measurement $\mathbf{d}$ would be a random variable characterized by a PDF, $\pi(\mathbf{d}|\boldsymbol{\theta})$. Therefore, it is important to understand the source of its randomness (i.e. lack of information). The sources of deviations are the measurement noise in the data and incompleteness (error) of the computational model.

Here it is assumed that the error in data and model are characterized by a zero mean Gaussian with unknown variances. Therefore, in addition to the (physical) parameters of the damage model, there are two random variables, Σ^2_{load} and Σ^2_{disp} (unknown variances), that can be interpreted as a measure of the overall discrepancy between the measured load $f_{\mathrm{exp}}(t^{(k)})$ and displacement $u_{\mathrm{exp}}(t^{(k)}; \mathbf{x})$ and the corresponding quantities computed with the damage models ($f_{\mathrm{model}}(t^{(k)})$ and $u_{\mathrm{model}}(t^{(k)}; \mathbf{x})$) (see [24] for more detailed information).

The corresponding likelihood model is then:

$$\begin{aligned}
\ln(\pi_{\mathrm{like}}(\mathbf{d}|\boldsymbol{\theta})) &= \frac{1}{2}\ln(2\pi) - N_t \ln(\Sigma_{\mathrm{load}}) - N_t N_x \ln(\Sigma_{\mathrm{displ}}) + \\
&- \frac{1}{2}\sum_{k=1}^{N_t}\left\{\left[\frac{f_{\mathrm{exp}}(t^{(k)}) - f_{\mathrm{model}}(E, s, \epsilon_{\mathrm{R}}; t^{(k)})}{\Sigma_{\mathrm{load}}}\right]^2 + \right. \\
&\qquad \left. + \sum_{i=1}^{N_x}\left[\frac{u_{\mathrm{exp}}(t^{(k)}, \mathbf{x}) - u_{\mathrm{model}}(E, s, \epsilon_{\mathrm{R}}; t^{(k)}, \mathbf{x})}{\Sigma_{\mathrm{displ}}}\right]^2\right\},
\end{aligned}$$

where according to the experiments:

- $N_t = 4$ = number of time steps used,
- $N_x = 91$ = number of "x" positions used,
- $f(t)$ = applied load at instant "t", and
- $u(t, \mathbf{x})$ = displacement of the specimen at instant "t" and position "$\mathbf{x}$".

The statistical inverse problem for calibrating the model parameters is conducted using the QUESO [4] [9] software package. Algorithms in the QUESO library require the prescription of a likelihood routine for statistical inverse problems.

6.2 Numerical Simulations and results

As indicated in Section 4, (26) provides the means to calibrate the damage model parameters against conducted experimental data accounting for the uncertainty in data and model parameters as well as real time monitoring of the damage variable. In this regard, an additional code (i.e. so called Top Application) is developed in this study that deals with the definition of statistical inverse problems (parameter spaces, prior PDFs, likelihood functions, reference data), as well as with the proper use of QUESO C++ classes in order to solve such statistical inverse problems through Bayesian formula. These application level routines provide the bridge between the statistical algorithms in QUESO, continuum damage model library, and conducted experimental data[5].

As indicated previously, using the Bayesian calibration process, the training data converts the initial knowledge about the parameters to *a posterior* density, revising out opinion about the true values of the parameters. In the other word, the effect of the experimental observation is to sharpen the posterior density, causing it to peak near the true values of the parameters. Figure 10 shows the computed posterior marginal kernel density estimation (KDE) of the parameters for Krajcinovic damage models as well as covariances Σ_{load} and Σ_{disp}. This figure shows that the measured data set $\mathbf{d}(t^{(k)}, \mathbf{x}) = \left\{u(t^{(k)}, \mathbf{x}), f_{\text{exp}}(t^{(k)})\right\}$, transforms the uniform prior PDF of (28) to the densities peaking around $2-3.5$ GPa, $0-0.2$, and 0.025, for E, s, and ϵ_{R} respectively. In this figure, the large width of the posterior marginal KDE of the modulus of elasticity, E, indicates that this model parameter is less informed by the training data (i.e. measurements). Also, the minimum uncertainty is observed about the ϵ_{R} among the physical damage model parameters since it is sharply peaked at 0.025. Moreover, the calculated and measured load has a low discrepancy than the one for the displacement. This can be due to the larger noise introduced by DIC to measure the spatial displacement.

In order to statistically evaluate how the scalar damage field develops with time throughout a volume region of the material, the extended Kalman filter is applied on the damage model. In the filtering approach, a model update happens in a real-time fashion. Thus, the damage model is given the opportunity to relearn from newer collected data, and adjust itself to the current provided information. In this regard, the material parameters of the damage models are fixed with the Maximum a Posterior (MAP) Estimation[6] values obtained from the statistical calibration results (Figure 10) and filtering process is conducted on the

[4]Quantification of Uncertainty for Estimation, Simulation and Optimization (QUESO) is an in-house package developed at the Institute for Computational Engineering and Science at the University of Texas at Austin. It is a collection of C++ classes and algorithms to support model validation and the prediction of quantities of interest with uncertainty quantification (UQ) included [9].

[5]In the current analyses, parallel computing is used in all computational steps. More specifically, Lonestar computational platform at the Texas Advanced Computing Center (TACC [28]) is employed, where each computational node contains 24 GB of memory and 12 processing cores of 2GHz each.

[6]MAP for $\boldsymbol{\theta}$ is defined as $\hat{\boldsymbol{\theta}} = \arg\max_{\boldsymbol{\theta}} \pi_{\text{post}}(\boldsymbol{\theta})$

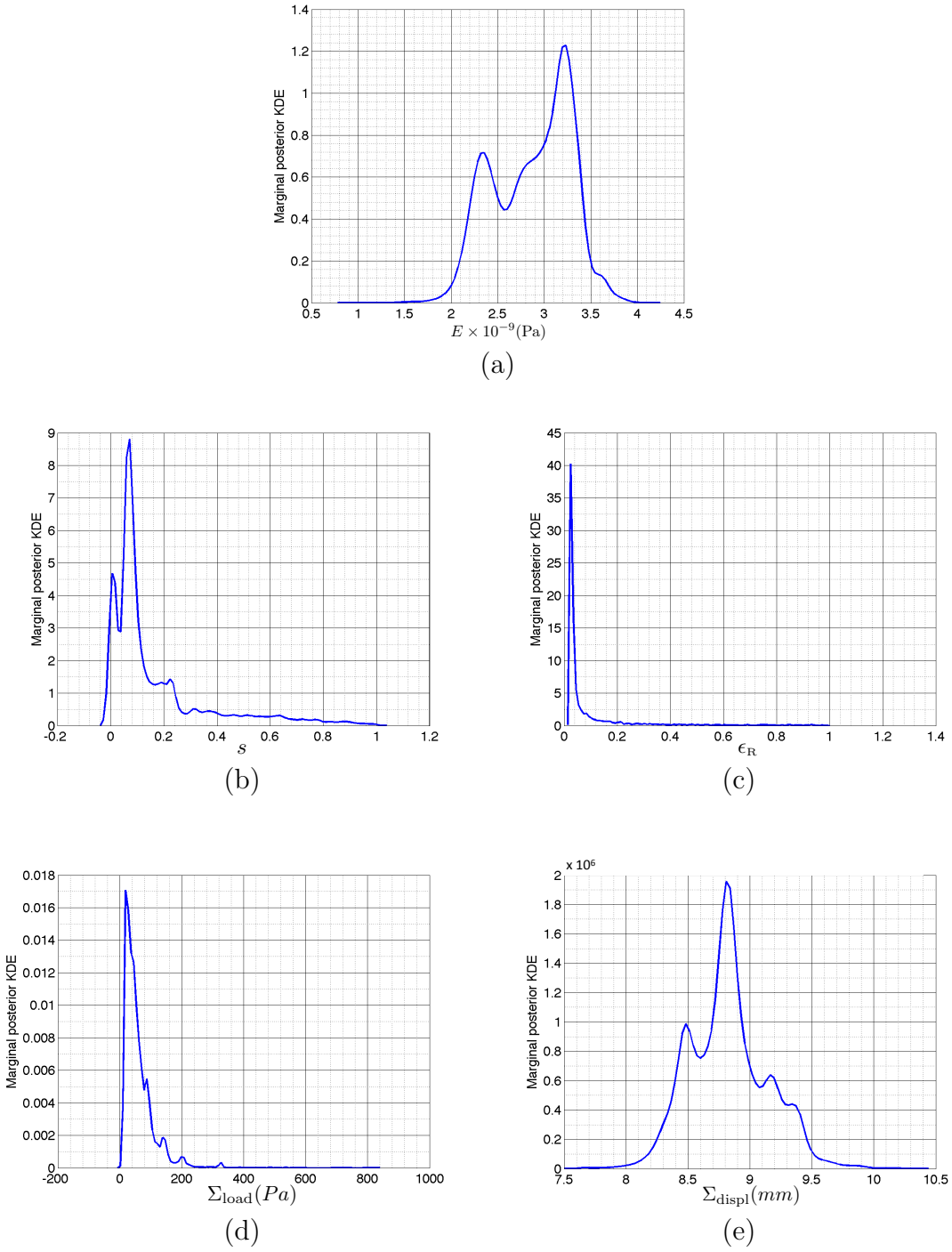

Figure 10: Calibrated material parameters for Krajcinovic damage model. Posterior marginal density estimation of (a) Elastic modulus; (b) parameter s; (c) parameter ϵ_{R}; (d) Σ_{load}; and (e) Σ_{disp}.

damage variable, $\boldsymbol{\theta} = D$ in (26), throughout the finite element mesh.

Figures 11 and 12 show the results of filtering the damage variables in term of spatial and

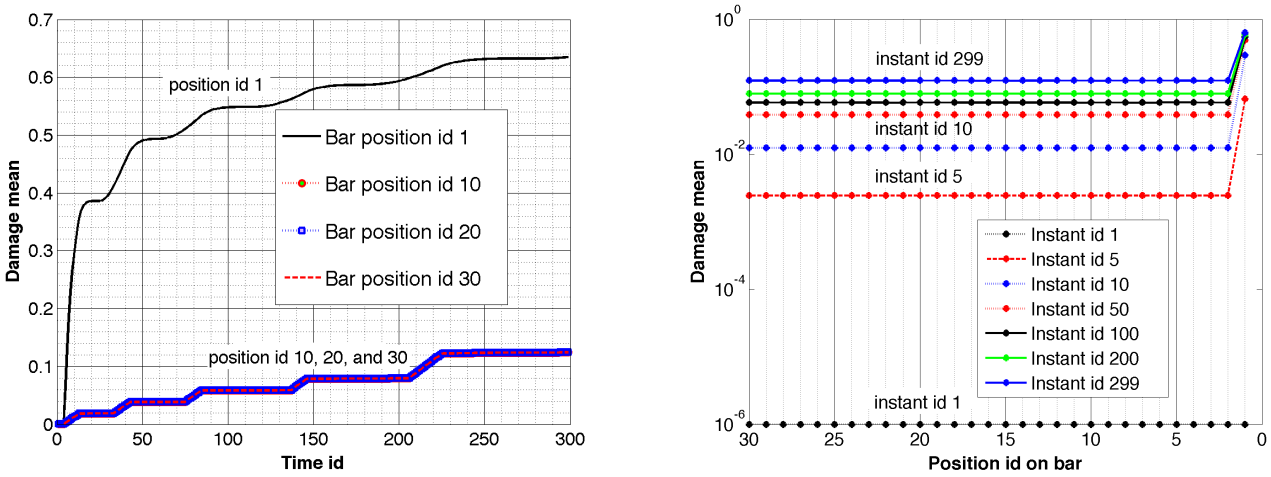

(a) (b)

Figure 11: Evolution of damage mean vector for Krajcinovic damage model with respect to (a) time $t^{(k)}$; (b) position x_i.

temporal variation of the damage mean vector and covariance matrix using the Krajcinovic damage model and the experimental data. The accumulation of damage during loading and unchanged value of the damage variable throughout the set of elastic unloading and reloading can be observed from these figures. Moreover, the results presented in Figure 11 indicate that higher rate of damage growth (material degradation) at the initial stage of the test in the *position id 1*. As indicated in Figure 9(a), this is the location of the observed *hot spot* in the experiment leading to the material failure. Moreover the overall decrease in the damage covariance matrix with respect to time shown in Figure 12 indicates the through the Bayesian filtering, observing additional measurements increases the level of confidence regarding the damage evolution. This is referred to as *Bayesian learning*, where learning goes on as the data are collected [8]. Therefore the developed DDDAS infrastructure enables one to forecast the failure in the system given the near "real" time data, so that one can be informed for potential decisions to be taken about the system, and/or for potential control actions to be taken.

7 Summary and Conclusions

The present study employ the mathematical models of material damage with the experimental characterization of the degradation in nanocomposite materials with in a Bayesian framework that allows the quantification and measurement of uncertainties in experimental data, and model parameters. The physical problem under study is the behavior of thin composite structural components such as are common in aircraft structures under loads that can generate distributed damage. Uniaxial tensile experiments with different load levels and including loading-unloading cycles are conducted on carbon nanotube infused epoxy nanocomposites specimens. The global response of the specimen, in the sense of generating distributed and progressive damage in different parts of the specimen, is initially charac-

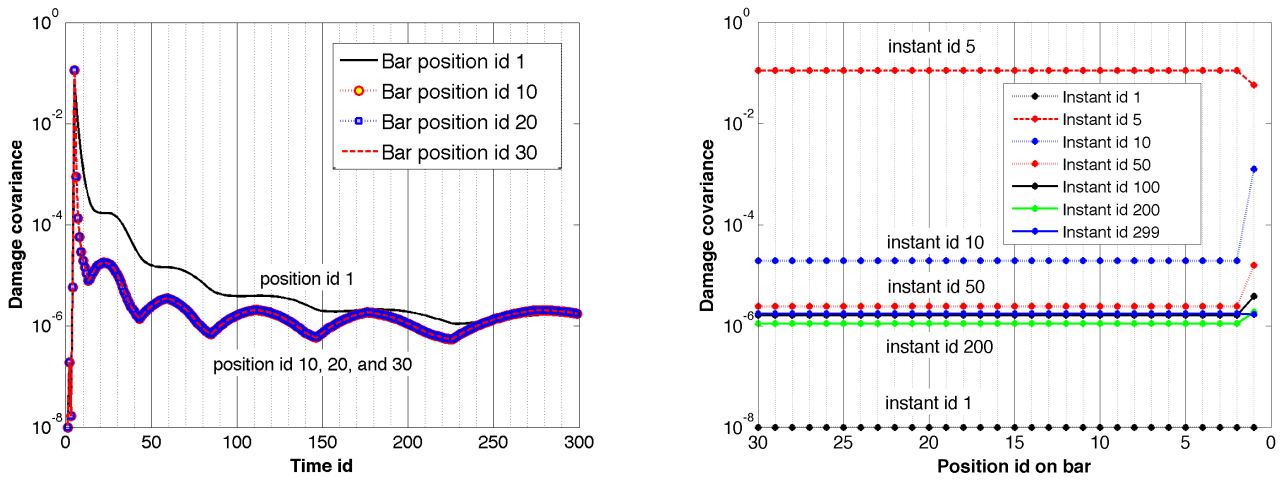

(a) (b)

Figure 12: Evolution of damage covariance matrix for Krajcinovic damage model with respect to (a) time $t^{(k)}$; (b) position x_i.

terized by the force and extension measurements. The spatial variation in the strain field (resulting from local perturbations in material state and properties) over time is measured using digital image correlation. In order to provide information for real-time monitoring of damage, the direct and indirect measurement of damage and degradation is made possible through an embedded CNT network in the matrix of the composite. The local damage in the form of micro-cracks is manifested as a change in the effective resistivity of the material. Therefore the damage and degradation in the material can be measured directly using the strain field and indirectly through the fluctuation in the resistivity. However, a direct correlation between the change in resistivity of the CNT composite and the damage evolution could not be established; therefore, direct measurement of strain variation was used as an indication of damage evolution. A general thermodynamically consistent framework is presented for characterizing the damage and degradation in the material. The damage evolution equitation suggested by Krajcinovic and Foneska [16] is taken into account in order to conduct the statistical calibration of the continuum damage mechanics model against the experimental data. Moreover, a Bayesian framework for calibration model with quantification of uncertainties is described in this work. A software infrastructure is developed and implemented in order to integrate the aforementioned constituents which incorporates: The numerical algorithms for a finite element solution of the continuum damage models; Generated experimental data; and Algorithms for sampling as well as model calibration based on Bayesian methods.

The results indicate that the Bayesian framework used in this study enables statistical calibration of the computational models of physical phenomena (i.e. continuum damage models) against experimental observations, along with quantifying the inherent uncertainties in the data, the model parameters, and the numerical solution approach.

Acknowledgments

The support of this work under AFOSR contract FA9550-11-1-0314 is gratefully acknowledged.

References

[1] M Balask, I Veres, Gy Molnr, Zs Balask, and E Svb. Composite structure of helicopter rotor blades studied by neutron- and x-ray radiography. *Physica B: Condensed Matter*, 350(13):107 – 109, 2004. Proceedings of the Third European Conference on Neutron Scattering.

[2] James O. Berger. *Statistical Decision Theory and Bayesian Analysis*. Springer Series in Statistics, 1985.

[3] Dan G. Cacuci. *Sensitivity and Uncertainty Analysis: Theory*, volume 1. CRC Press, 2007.

[4] J. L. Chaboche. Continuum damage mechanics: Part I - General concepts. *Journal of Applied Mechanics*, 55:59–64, 1988.

[5] J. L. Chaboche. Continuum damage mechanics: Part II - Damage growth, crack initiation and crack growth. *Journal of Applied Mechanics*, 55:65–72, 1988.

[6] F.C. Beer de, M. Coetzer, D. Fendeis, A. Costa Da, and M.E. Silva. Neutron radiography and other NDE tests of main rotor helicopter blades. *Applied Radiation and Isotopes*, 61:609 616, 2004.

[7] Babur Deliktas, George Z. Voyiadjis, and Anthony N. Palazotto. Simulation of perforation and penetration in metal matrix composite materials using coupled viscoplastic damage model. *Composites Part B: Engineering*, 40(6):434 – 442, 2009. Blast/impact on engineered (nano)composite materials.

[8] R. O. Duda, P. E. Hart, and D. G. Stork. *Pattern Classification (2Nd Edition)*. Wiley-Interscience, 2000.

[9] K. C. Estacio-Hiroms and E. E. Prudencio. *Quantification of Uncertainty for Estimation, Simulation, and Optimization (QUESO), User's Manual*. Center for Predictive Engineering and Computational Sciences (PECOS), Institute for Computational and Engineering Sciences (ICES), The University of Texas at Austin, Austin, TX 78712, USA, version 0.45.3 edition, October 2012.

[10] W. Harizi, S. Chaki, G. Bourse, and M. Ourak. Mechanical damage assessment of glass fiber-reinforced polymer composites using passive infrared thermography. *Composites Part B: Engineering*, 59(0):74 – 79, 2014.

[11] N. Heeder, A. Shukla, V. Chalivendra, and S. Yang. Sensitivity and dynamic electrical response of cnt-reinforced nanocomposites. *Journal of Materials Science*, 47(8):3808–3816, 2012.

[12] L. M. Kachanov. On time to rupture in creep conditions. *Izviestia Akademii Nauk SSSR*, 8:26–31, 1958.

[13] Jari Kaipio and Erkki Somersalo. *Statistical and Computational Inverse Problems*. Springer, 2005.

[14] K. Kanatani. Distribution of directional data and fabric tensors. *International Journal of Engineering Science*, 22(2):149 – 164, 1984.

[15] B. S. Kirk, J. W. Peterson, R. H. Stogner, and G. F. Carey. libMesh: a C++ library for parallel adaptive mesh refinement/coarsening simulations. *Engineering with Computers*, 22(3):237–254, 2006.

[16] D. Krajcinovic and G. U. Fonseka. The continuous damage theory of brittle materials, Parts 1 and 2. *Journal of Applied Mechanics*, 48:809–824, 1981.

[17] Sunghee Lee, Taehyo Park, and George Z. Voyiadjis. Free vibration analysis of axially compressed laminated composite beam-columns with multiple delaminations. *Composites Part B: Engineering*, 33(8):605 – 617, 2002.

[18] J. Lemaitre and J. L. Chaboche. *Mechanics of Solid Materials*. Combridge University Press, 1990.

[19] V.A. Lubarda and D. Krajcinovic. Damage tensors and the crack density distribution. *International Journal of Solids and Structures*, 30(20):2859 – 2877, 1993.

[20] John Montesano, Habiba Bougherara, and Zouheir Fawaz. Application of infrared thermography for the characterization of damage in braided carbon fiber reinforced polymer matrix composites. *Composites Part B: Engineering*, 60(0):137 – 143, 2014.

[21] E.V. Morozov, S.A. Sylantiev, and E.G. Evseev. Impact damage tolerance of laminated composite helicopter blades. *Composite Structures*, 62(34):367 – 371, 2003.

[22] S. Murakami and N. Ohno. *Continuum theory of creep and creep damage*. Springer, 1981.

[23] NASA. Carbon Nanotube-Based Structural Health Monitoring Sensors, 2011. NASA Tech Briefs, LAR-16475-1.

[24] E. E. Prudencio, P. T. Bauman, D. Faghihi, K. Ravi-Chandar, and J. T. Oden. A computational framework for dynamic data-driven material damage control, based on bayesian inference and model selection. *International Journal for Numerical Methods in Engineering*, 2014. doi:10.1002/nme.4669.

[25] J. Rausch and E. Mäder. Health monitoring in continuous glass fibre reinforced thermoplastics: Tailored sensitivity and cyclic loading of CNT-based interphase sensors. *Composites Science and Technology*, 70:2023–2030, 2010.

[26] Thanyawalai Sujidkul and Zhenhai Xia. Coupled thermalmechanical modeling of carbon fibers reinforced polymer composites for damage detection. *Composites Part B: Engineering*, 43(3):1631 – 1636, 2012.

[27] MA Sutton, WJ Wolters, WH Peters, WF Ranson, and SR McNeill. Determination of displacements using an improved digital correlation method. *Image and Vision Computing*, 1(3):133 – 139, 1983.

[28] Texas Advanced Computing Center TACC. `http://www.tacc.utexas.edu/`, 2008-2012.

[29] A. Tarantola. *Inverse Problem Theory and Methods for Model Parameter Estimation*. SIAM, 2005.

[30] Erik T. Thostenson and Tsu-Wei Chou. Carbon nanotube-based health monitoring of mechanically fastened composite joints. *Composites Science and Technology*, 68(12):2557 – 2561, 2008.

[31] Venkat K. Vadlamani, Vijaya B. Chalivendra, Arun Shukla, and Sze Yang. Sensing of damage in carbon nanotubes and carbon black-embedded epoxy under tensile loading. *Polymer Composites*, 33(10):1809–1815, 2012.

[32] Christian Viets, Simon Kaysser, and Karl Schulte. Damage mapping of GFRP via electrical resistance measurements using nanocomposite epoxy matrix systems. *Composites Part B: Engineering*, In Press.

[33] George Z. Voyiadjis and Babur Deliktas. Damage in {MMCs} using the gmc: theoretical formulation. *Composites Part B: Engineering*, 28(56):597 – 611, 1997.

[34] George Z. Voyiadjis, Babur Deliktas, and Anthony N. Palazotto. Thermodynamically consistent coupled viscoplastic damage model for perforation and penetration in metal matrix composite materials. *Composites Part B: Engineering*, 40(6):427 – 433, 2009. Blast/impact on engineered (nano)composite materials.

[35] G.Z. Voyiadjis and A.H. Almasri. Experimental study and fabric tensor quantification of micro-crack distributions in composite materials. *Journal of Composite Materials*, 41(6):713 – 745, 2007.

[36] G.Z. Voyiadjis and P.I. Kattan. Damage mechanics with fabric tensors. *Mechanics of Advanced Materials and Structures*, 13(4):285 – 301, 2006.

[37] G.Z. Voyiadjis and P.I. Kattan. A new fabric-based damage tensor. *Journal of the Mechanical Behaviour of Materials*, 17(1):31 – 56, 2006.

[38] G.Z. Voyiadjis, P.I. Kattan, and Z.N. Taqieddin. Continuum approach to damage mechanics of composite materials with fabric tensors. *International Journal of Damage Mechanics*, 16(3):301 – 329, 2007.

[39] G.Z. Voyiadjis, Z.N. Taqieddin, and P.I. Kattan. Micromechanical approach to damage mechanics of composite materials with fabric tensors. *Composites Part B: Engineering*, 38(78):862 – 877, 2007.

[40] Jie Wen, Zhenhai Xia, and Fred Choy. Damage detection of carbon fiber reinforced polymer composites via electrical resistance measurement. *Composites Part B: Engineering*, 42(1):77 – 86, 2011.

[41] Robert Winkler. *An Introduction to Bayesian Inference and Decision*. Probabilistic Publishing, 2003.